Microscopic insight into the impact of the KF post-deposition treatment on optoelectronic properties of (Ag,Cu)(In,Ga)Se$_2$ solar cells

Maximilian Krause, José A. Márquez, Sergej Levcenko, Thomas Unold, Olivier Donzel-Gargand, Marika Edoff, Daniel Abou-Ras

1 Helmholtz-Zentrum Berlin für Materialien und Energie GmbH, Hahn-Meitner-Platz 1, 14109 Berlin, Germany;

2 Solar Cell Technology, Department of Material Science and Engineering, Uppsala University, SE-751 21 Uppsala, Sweden

Abstract

It is attractive to alloy Cu(In,Ga)Se$_2$ solar-cell absorbers with Ag (ACIGSe), since they lead to similar device performances as the Ag-free absorber layers, while they can be synthesized at much lower deposition temperatures. However, a KF post-deposition treatment (PDT) of the ACIGSe absorber surface is necessary to achieve higher open-circuit voltages (V_{oc}). The present work provides microscopic insights to the effects of this KF PDT, employing correlative scanning-electron microscope techniques on identical positions of cross-sectional specimens of the cell stacks. We found that the increase in V_{oc} after the KF PDT can be explained by the removal of Cu-poor, Ag-poor, and Ga-rich regions near the ACIGSe/CdS interface. The KF PDT leads, when optimally doped, to a very thin K-Ag-Cu-Ga-In-Se layer between ACIGSe and CdS. If the KF dose is too large, we find that Cu-poor and K-rich regions form near the ACIGSe/CdS interface with enhanced nonradiative recombination which explains a decrease in the V_{oc}. This effect occurs in addition to the presence of a (K,Ag,Cu)InSe$_2$ intermediate layer, that might be responsible for limiting the short-current density of the solar cells due to a current blocking behavior.

1. Introduction

Thin-film solar cells based on Cu(In,Ga)Se$_2$ (CIGSe) absorber layers have reached efficiency levels of well above 23%[1]. In the recent years, it has become a focus of research to alloy the CIGSe absorbers with Ag, mainly since their synthesis is possible at lower deposition temperatures[2] than for the quaternary CIGSe layers, i.e., leading to lower production costs, while still high conversion efficiencies can be achieved,[3,4] featuring particularly high open-circuit voltages (V_{oc}) of the devices.

In addition, KF post-deposition (PDT) treatments of the Ag-containing CIGSe (ACIGSe) absorbers were demonstrated to be beneficial for the solar-cell performance of the corresponding devices. When using CdS buffer layers deposited by a chemical bath, their coverage of the absorber surface treated by KF was improved, and therefore, it was possible to decrease the CdS layer thicknesses[5,6], resulting in increased short-circuit current densities, owing to lower series resistances and reduced parasitic absorption in the CdS layer.[7]
In a recent work by Donzel-Gargand et al.,[8] it was shown that a KF post-deposition treatment (PDT) of the Ag-containing CIGSe layer is necessary to improve the V_{oc} and fill factor (FF) of the corresponding solar cells substantially. These authors also reported that the photovoltaic parameters are improved up to a specific KF concentration and that higher concentrations lead to a substantial deterioration of the conversion efficiency. Since these

authors did not conduct sufficient analysis to conclude on possible origins for the effects of the KF PDT, we performed these investigations in the present contribution.

Correlative microscopic analyses were conducted applying various characterization techniques in a scanning electron microscope (SEM) on identical cross-section areas, enhancing the information obtained from the individual measurement. The three ACIGSe solar cells already investigated by Donzel-Gargand et al.[8] were analyzed, i.e., a solar cell without any KF PDT after the ACIGSe deposition ("No KF") as reference, as well as two devices with an optimal KF concentration ("Optimal KF") and with KF provided in excess ("Extra KF"). We show that in the solar cell without KF PDT, considerable electrostatic potential fluctuations were found. These fluctuations can be attributed to inhomogenously distributed, Cu-depleted Ag-Cu-In-Ga-Se precipitates located at the CdS/ACIGSe interface and cause substantial V_{oc} losses. An optimized KF concentration reduces compositional inhomogeneities at the CdS/ACIGSe interface successfully, thus, a remarkable increase in V_{oc} and FF is achieved. In case the KF concentration is too high, extended secondary phases form at the CdS/ACIGSe interface, which deteriorate all photovoltaic parameters.

2. Methods

Solar cell devices were processed according to the description in Ref. 8. K-rich/Na-poor glass substrates were coated by molybdenum (400 nm) and a NaF precursor layer (15 nm). The ACIGSe absorber layers were deposited by a three-stage process (Cu-poor/ Cu-rich/ Cu-poor), followed by a KF PDT for the Optimal KF and Extra KF samples. The KF dose for the Extra KF sample was five times higher than for the Optimal KF sample. Subsequently, a CdS a buffer layer (30-50 nm) was deposited by a chemical bath. An i-ZnO layer (80nm) as well as a ZnO:Al (300 nm) were sputtered via radio-frequency magnetron sputtering. Finally, a Ni/Al/Ni metal grid for enhanced collection at the front contact was evaporated. The concentration ratio in the ACIGSe absorbers of group I elements, [Ag]/([Ag]+[Cu]) (AAC), was about 0.18, that of group III elements, [Ga]/([Ga]+[In]) (GGI), about 0.4, and the ([Ag]+[Cu])/([Ga]+[In]) ration about 0.XX which quantifies the stoichiometry level.

For SEM analyses, cross-sectional specimens from the solar-cell stacks were prepared by face-to-face gluing of two solar cells and mechanical polishing of the cross-sections. Specimens characterized by electron backscatter diffraction (EBSD), energy-dispersive X-ray (EDX) and cathodoluminescence (CL) spectroscopy were additionally polished by Ar-ion milling. A very thin (nominally 5 nm) carbon layer was evaporated on the cross-section surfaces. All measurements were conducted at room temperature. The characterization by means of EBSD, CL, and EDX was carried out using Zeiss UltraPlus and Zeiss Merlin scanning electron microscopes, which are equipped with Oxford Instruments NordlysNano EBSD and UltimExtreme EDX detectors, as well as with a DELMIC SPARC CL system. The EBSD measurements were performed at 20 keV and about 1 nA. EBSD patterns were acquired at point-to-point distances of 50 nm and evaluated using the Oxford Instruments HKL software packages AZtec and CHANNEL5. A tetragonal crystal structure was used for indexing the EBSD patterns. Spatially resolved CL measurements were performed at room temperature at a beam energy of 10 keV and a beam current of 750 pA, using an InGaAs array detector. Elemental distribution maps were acquired at 7 keV and evaluated by the AZtec software suite (Oxford Instruments).

C-V measurements were performed at room temperature in the dark using a HP 4284A LCR-Meter, at frequencies of 10 kHz and 1000 kHz, and applying the 4-point probe method. The

capacitance values were calculated assuming a simple parallel RC circuit. External quantum efficiency (EQE) of solar cells was acquired with a lock-in amplifier. A chopped white light source (900 W, halogen lamp, 280 Hz) and a dual grating monochromator generated the probing beam. The beam size was adjusted such that the illumination area was smaller than the device area, and white bias light was applied.

Absolute PL measurements were conducted in a home built hyperspectral imaging setup. The full area of the samples was excited optically using monochromatic light from two 660 nm lasers coupled to homogenizer units. The excitation beam was adjusted to be equivalent to 1-sun conditions for an assumed, step-like absorptivity corresponding to a band-gap energy of ~1.1 eV (2.8×10^{21} photons m^{-2} s^{-1}). Spectral resolution of the PL images was obtained using a liquid crystal, tunable filter with a wavelength step size of 10 nm. The PL images from 900 to 1700 nm were taken via a peltier-cooled InGaAs camera in a system calibrated to absolute photon numbers.

3. Results

3.1. Solar-cell performances

Table 1 summarizes the median photovoltaic parameters of the three investigated samples. It is apparent that applying a KF PDT treatment leads to a decrease of the short-circuit current density (j_{sc}), while V_{oc} and *FF* are increased. On the other hand, providing KF in excess leads to an overall deterioration of the solar-cell parameters.

Table 1: Solar cell parameters (open-circuit voltage V_{oc}, short-circuit current density j_{sc}, fill factor FF and the power conversion efficiency η) of the investigated ACIGSe devices with various KF PDT at the same ACIGSe absorber. Here, we show the average values of 10 measured solar cells of each type according to Ref. [8] *(total area; without anti-reflective coating).*

	V_{oc} (mV)	j_{sc} (mAcm^{-2})	FF (%)	η (%)
No KF	728	31.2	71	16.1
Optimal KF	776	30.6	72	17.1
Extra KF	503	24.8	38	4.7

3.2 (Ag,Cu)(In,Ga)Se$_2$ bulk characteristics

Since the ACIGSe absorber layers in the three investigated solar cells were not deposited in the identical production run, we first verified that microstructures and elemental distributions of these layers are similar, i.e., that we can conclude on the effects of KF PDT applied on

same ACIGSe/Mo thin-film stacks. (We assume that the subsequently deposited CdS/i-ZnO/ZnO:Al buffer/window layers are same for all three samples.)
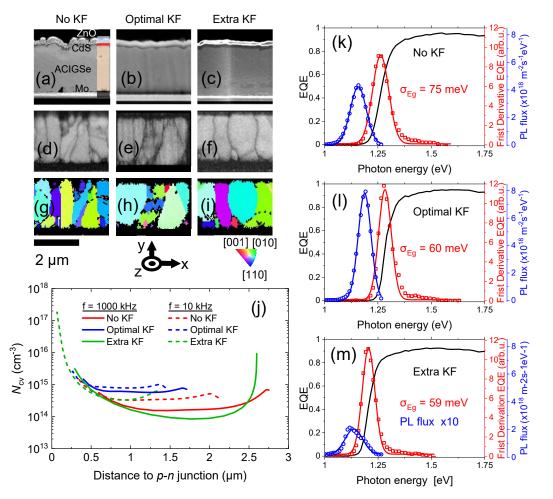

Figure 1: Cross-sectional SEM images (a,b,c), EBSD pattern-quality maps (d,e,f), and EBSD orientation-distribution maps (g,h,i) with respect to substrate (z axis) shown for ACIGSe solar cells with various KF-PDTs. j: Apparent net-doping profiles N_{CV} vs. the distance to the p-n junction acquired at a frequency of 10 kHz (dashed) and 1000 kHz (solid). The area of each solar cell was 0.5 cm². k, l, m: EQE spectra (black) and the first derivatives of the EQE spectra (red dots) as well as the average, absolute PL spectra (blue dots) acquired on the identical solar cells at excitations equivalent to one sun. The first derivatives of the EQE and the PL spectra were fitted using a Gaussian shown as solid lines in blue and red. The PL flux for Extra KF sample is multiplied by factor 10.

3.2.1 Microstructure

EBSD maps were acquired on cross-sectional areas of up to 150 μm in width. From these data sets, information on grain-size distributions and preferential crystal orientations were extracted. The average grain sizes in all three ACIGSe were about 0.6 μm, independent of the KF concentration in the PDT (Figure S1). In addition, no preferred crystal orientation was detected in any of the ACIGSe layers. It is interesting to note that the maximum detected

grain size was largest for the ACIGSe layer in the Extra KF sample. Nevertheless, overall, the EBSD measurements (EBSD pattern-quality map, EBSD orientation map, and corresponding cross-sectional SEM images, Figure 1a-i) did not indicate any substantial difference in the microstructure of the three ACIGSe thin films, and therefore, also any indication of an impact of the KF-PDT on this film property.

3.2.2 Elemental distributions

As already reported in Ref. 8, the Ga gradients in all three ACIGSe thin films exhibit strong slopes towards the back contact, but remain rather flat everywhere else. We confirmed these distributions of the Ga gradients by EDX spectroscopy (see supplementary information, Figure S2) and also by the CL analysis further below (Figure S6). The concentration ratios of group I elements, AAC, remain constant throughout the ACIGSe layers with a slight decrease towards the Mo back contact.

Based on the results presented so far, it can be concluded that microstructure and elemental distributions in the ACIGSe bulk are the same for all three investigated samples, however, the Extra KF sample exhibits a slightly lower band-gap energy owing to a reduced Ga concentration at the front interface. Therefore, it is valid to attribute differences in the electrical and optoelectronic properties of the ACIGSe layers and of the completed solar cells to the different KF-PDTs applied.

3.2.3 Net-doping densities

To verify the doping densities N_{CV} in the ACIGSe absorber layers with various KF-PDTs, C-V measurements were performed on the solar cells. Figure 1j shows the dependencies of N_{CV} versus the distance to the *p-n* junction, calculated by $x = \varepsilon_r \varepsilon_0 A/C$ (where ε_r (assuming 13.6 for CuInSe$_2$ [9]) and ε_0 are the dielectric susceptibilities of ACIGSe and the vacuum, A is the area of the solar cell, 0.5 cm^{-2}, and C is the capacitance). Apparently, changes in the N_{CV} profiles by varying the applied frequency from 10 kHz to 1000 kHz are noticeable. Variation according to the frequency are attributed to additional response of defects at low frequency.[10] Here, the Optimal KF sample reveals rather small changes which indicates a lower defect density in compare to the No and Extra KF devices.

The net-doping densities p_0 obtained from the of N_{CV} were 3×10^{14}, 6×10^{14}, and 1×10^{14} cm^{-3} at 1 MHz for the No KF, Optimal KF, and Extra KF samples. However, it is worth noting that the given values are rough estimates as the capacitance response of these cells at high frequency approaches the geometrical capacitance. C-V measurements on other ACIGSe solar cells with similar AAC and GGI ratios[11,12] in the ACIGSe layers also provided net-doping densities on the order of 10^{14}-10^{15} cm^{-3}. We note that the Optimal KF sample exhibits a net-doping density slightly larger than for the other two samples, and that the value for the Extra KF is smaller than for the No KF sample. Both trends were reported as a result of K doping in CIGSe solar cells.[6,13]

3.2.4 Absolute PL imaging and EQE

Figures 1k-m show the EQE spectra (black), their first derivatives (red), and the absolute PL spectra (blue) from the three samples, acquired on full devices (the PL intensity is given as absolute photon flux Y_{PL}). The PL spectra as well as the first derivatives were fitted by Gaussians, of which the resulting center emission/absorption energies are summarized in Table 2. While the peak values of the first derivatives can be identified with the band-gap energies, the maxima in the PL signals are systematically smaller than the band-gap energies. This shift between the peaks in the first derivatives and the PL signal is a well-known phenomenon and has been also observed in CIGSe[14] and may be related to band-gap grading in the ACIGSe alloy. The band-gap energy of the Extra KF sample is slightly smaller than those of the other two samples, which is in good agreement with the slightly smaller [Ga] as visible in Figure S2.

The disorder in the ACIGSe alloy can be modeled in terms of the amplitude of band-gap fluctuations which is equal to the standard deviation σ of the Gaussian distribution fitted to the first derivatives of the EQE spectra. According to Rau $et\ al.$[15], the V_{oc} losses due to band-gap fluctuations can be estimated via $V_{oc,loss} = \sigma^2 / 2ek_BT$. We obtained the values of 112, 72, and 70 mV for the No KF, Optimal KF, and Extra KF samples. This is, the band-gap fluctuations are reduced when applying a KF PDT. Indeed, as we will see further below, the No KF exhibits secondary phases on the ACIGSe side of the ACIGSe/CdS interface that are not present anymore in the Optimal KF and and Extra KF samples.

Using the approach provided by Redinger $et\ al.$,[16] assuming that $Y_{PL} / Y_{ill} = B\ p_0\ \tau$, with B the radiative recombination coefficient (1×10^{-11} cm^{3}s^{-1})[16], p_0 the net-doping density from Sec. 3.2.3, and Y_{ill} the flux of the incoming laser beam, minority-carrier lifetimes of 170, 175, and 50 ns were calculated for the No KF, Optimal KF, and Extra KF samples. However, the value of B was determined for CuInSe2, and the corresponding value for ACIGSe, which is not available in the literature, can differ substantially. Therefore, we do not consider the absolute values but only the relative differences of the lifetimes, noting that the lifetime in the Extra KF sample is much smaller than in the No KF and Optimal KF samples.

The average external PL quantum yield (PLQY) for the samples and corresponding nonradiative $V_{OC,loss}$[17] is given in Table 2. Apparently, the Optimal KF sample performs best. However, when calculating $\varDelta V_{OC}$, which takes into account the V_{OC} values at the Shockley-Queisser limit according to the band-gap energies acquired from EQE, it becomes even more obvious that the Extra KF sample is strongly limited by nonradiative recombination. On the other hand, the Optimal KF sample exhibits similar loss values as those reported recently for a high-efficient Cu(In,Ga)Se2 solar cell[18].

Table 2: Peak energies and corresponding full-width at half maximum (FWHM) in eV determined by fitting Gaussians to the first derivatives of the EQE spectra (dEQE/dE) and to the PL spectra (Figures 1k-m). As well as the PL quantum yield (PLQY) and the corresponding nonradiative $V_{OC,loss} = k_BT\ ln(PLQY)$[17]. The $V_{OC,SQ}$ are the V_{OC} values at the Shockley-Queisser limit[19] for band-gap energies equal to the EQE peak energies and the $\varDelta V_{OC} = V_{OC,SQ} - V_{OC,loss} - V_{OC,exp}$ (with the $V_{OC,exp}$ from Table 1).

	No KF	Optimal KF	Extra KF

dEQE/dE	Peak energy (eV)	1.26	1.28	1.20
	FWHM (eV)	0.07	0.06	0.06
PL	Peak energy (eV)	1.16	1.19	1.14
	FWHM (eV)	0.07	0.06	0.08
	PLQY (x10^{-4} %)	1.47	2.14	0.09
	$V_{OC,loss}$ (mV)	220	210	290
	$V_{OC,SQ}$ (mV)	1006	1025	950
	ΔV_{OC} (mV)	57	38	158

3.3 Impact of KF-PDT on the ACIGSe/buffer interface

In order to detect microscopic origins for the different photovoltaic performances of the solar cells with and without KF PDT, we analyzed the three samples by means of EDX, EBSD, and CL in cross-sectional geometry.

Elemental distribution maps acquired by EDX are given in Figure 2j-r (note that all EDX maps for all elements and corresponding SEM cross-section images are provided in Figures S3-S5 for the No KF, Optimal KF and Extra KF samples). From these maps, it is apparent that Cu-depleted regions are present on the ACIGSe sides of the CdS/ACIGSe interfaces for the No KF and Extra KF samples, while such regions are not visible in the Cu-distribution map of the Optimal KF sample, as shown in Figure 2j-r. On these Cu-depleted regions, Ga enhancement is found for the No KF sample, while for the Extra KF sample, these regions appear enriched in K. These elemental distributions suggest the presence of secondary phases in these Cu-depleted/Ga-enriched and Cu-depleted/K-enriched regions. Furthermore, Donzel *et al.* [8] applied transmission-electron microscope studies and revealed a very thin (view nm) layer of K-Ag-Cu-In-Ga-Se on the Optimal KF and a thicker layer on the Extra KF sample.
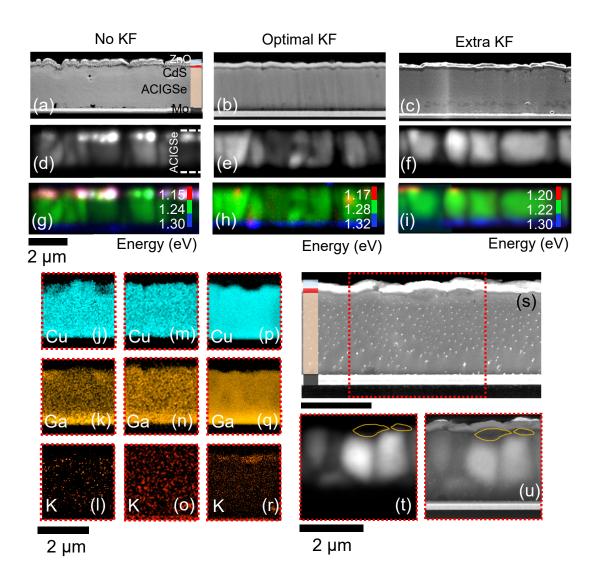
Figure 2: SEM cross-section images (a-c), CL intensity maps (d-f), and CL peak-energy maps with emission energy given by false color (g-h) shown for ACIGSe solar cells with various KF-PDTs. EDX elemental distribution maps using Cu-L (j,m,p), Ga-L (k,n,q), and K-K (l,o,r) X-ray lines acquired on the No KF (j-l), Optimal KF (m-o), and Extra KF (p-r) samples. The Cu depletion on the ACIGSe side of the ACIGSe/CdS interface is found for the No KF and Extra KF samples. The Extra KF sample exhibits an enhanced K signal where the Cu is depleted. At the identical cross-sectional position of the Extra KF sample a SEM image (s), a panchromatic CL-intensity map (t) is acquired on the area highlighted by a red, dashed rectangle in (s). The CL-intensity map superimposed on the SEM image (u). The locations of the secondary phases are marked by yellow lines in the CL map. On the cross-section surface in the SEM image, small dots are visible, which can be identified as Cu agglomerates as a result of the Ar-ion polishing.[20]

One feature common in all CL peak-energy maps (Figures 2g-i) is the larger emission energy close to the Mo back contact, which is due to the strong Ga gradient present in this region of the absorbers (see Figure 2 above as well as Figures S2-S5). These observations are also

shown by line scans from the CL peak-energy maps (Figure S6) and quantified by extracted point spectra. However, the secondary phases detected by the EDX analyses are also visible in CL hyperspectral images (Figure 2a-i). The CL map of the No KF sample exhibits areas near the CdS/ACIGSe interface with enhanced luminescence intensity and smaller emission-peak energies, which can be attributed to the Cu-depleted/Ga-enriched regions identified by EDX. The ACIGSe/CdS interface of the Extra KF sample shows areas without detectable CL signals (see Figure 2s-u; we also checked for CL signals in the range of 300-1400 nm). We attribute these regions to the Cu-poor/K-rich areas detected by means of EDX (Figures 2p-r and Figure S5).

We also extracted profiles across 20 different grain boundaries in each sample, in order to estimate the recombination velocities using an approach described in detail in Ref. 18. For this estimation, the lifetimes determined in Sec. 3.2.4. are required. The estimated, average grain-boundary recombination velocities were 250, 200, and 800 cm/s for the No KF, Optimal KF and Extra KF samples.
The comparison of the No KF and Optimal KF samples evidences that the treatment did not induce a significant impact in reducing recombination at grain-boundaries. However, since the lifetimes can be regarded only in a relative way the order of magnitude for the grain-boundary recombination velocities is for all three samples identical, including Extra KF.

4. Discussion

The KF PDT was found to affect the electrical and optoelectronic properties of the ACIGSe bulk. While the microstructures and elemental distributions are similar for the ACIGSe thin films studied in the present work, the PL intensities and also the estimated minority-carrier lifetimes were significantly higher for the No KF and Optimal KF samples, which can be attributed to the different secondary-phase distributions at the ACIGSe side of the ACIGSe/CdS interface for the three samples. In addition, the net-doping density was slightly larger for the Optimal KF than for the No KF and Extra KF samples, which has been reported as one possible effect of K-doping of CIGSe absorbers.[6]

The main effects of KF PDT are related to the ACIGSe/CdS interface region (see Figure 3 for a summary). Without any KF PDT, the ACIGSe side of the ACIGSe/CdS interface exhibits Cu-poor/Ga-rich regions. As first reported by Donzel-Gargand et al.[8] as well as by Edoff et al.[3], these regions are actually depleted in Cu and Ag. Since the CL peak energies of these regions are smaller than that of the ACIGSe bulk (see Figure S6), we can assume that also the band-gap energy in these regions is smaller, which would agree with a Ag-depleted stoichiometry, in case the Ga enrichment is not too extensive. Probably, these Ag-Cu-In-Ga-Se secondary phases between ACIGSe and CdS lead to an unfavorable band alignment between absorber and buffer, and thus, to enhanced recombination and decreased V_{oc} (Table 1), also influenced by a slight decrease in the band-gap energy, as compared with the Optimal KF sample. In contrast, the collection (j_{sc}) is slightly enhanced (Table 1) via enhanced absorption due to the smaller band-gap energy.

These Cu- and Ag-depleted phases are removed by the KF PDT, which can be interpreted as passivation of the absorber/buffer interface region. A K-Ag-Cu-In-Ga-Se intermediate layer (not necessarily contiguously, maybe only as islands) forms between ACIGSe and CdS, which was identified by Donzel-Gargand et al.[8] as enriched in K, Ag and In, and as monoclinic (K,Ag)InSe$_2$ (we stick to a K-Ag-Cu-In-Ga-Se compound in the present work,

since these elements were identified in the EDX analysis). As long as the thickness of this layer is very small (few nm), it has no current-blocking character. However, if its thickness becomes too large (as in the case of the Extra KF sample), the collection is substantially deteriorated. A second feature of the ACIGSe/CdS interface of the Extra KF sample are the Cu-poor/K-rich regions, in which we could not detect any CL signal. Our interpretation is that this phase might be responsible to the enhanced nonradiative recombination observed in this sample, which may be considered as one reason for the low V_{oc} in the Extra KF sample and might be also correlated to the lower band-gap energy.
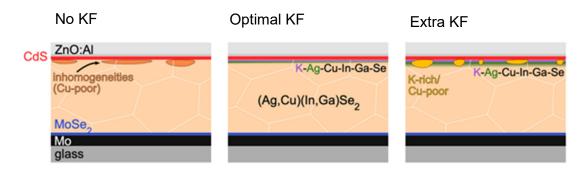

Figure 3: Schematic representation of the resulting ACIGSe stacking sequences for various KF-PDT. Inhomogeneities and precipitates are not drawn to scale.

5. Conclusion

In the present work, the effect of KF PDT on the materials and device properties of ACIGSe solar cells was studied employing correlative SEM techniques including also PL, EQE and C-V measurements. It was found that an optimized KF dose not only slightly increases the net-doping density of the ACIGSe layer but also removes Cu- and Ag-depleted (and Ga-enriched) areas in the ACIGSe/CdS interface region. In the ACIGSe solar cell produced without KF PDT, these areas exhibit a smaller band-gap energy, which is considered as detrimental for the device performance. On the other hand, the band alignment between the ACIGSe and the CdS is probably not favorable in case the Cu- and Ag-depleted areas are present, leading to enhanced interface recombination and thus lower V_{oc} than for a ACIGSe solar cell with optimized KF dose.

The ACIGSe/CdS interface region of the ACIGSe solar cell with optimized KF dose features a very thin (few nm) intermediate K-Ag-Cu-In-Ga-Se thin film. If the KF dose is too high, this intermediate layer becomes too thick and exhibits a current-blocking character. Moreover, extended secondary phases forms at the CdS/ACIGSe interface of the Extra-KF sample, which lead to enhanced nonradiative recombination and thus decreased V_{oc}. Therefore, all photovoltaic parameters are deteriorated for too high KF doses.

References

1. Nakamura, M. *et al.* Cd-Free Cu(In,Ga)(Se,S)$_2$ Thin-Film Solar Cell With Record Efficiency of 23.35%. *IEEE J. Photovoltaics* **9**, 1863–1867 (2019).
2. Chen, L., Lee, J. & Shafarman, W. N. The Comparison of (Ag,Cu)(In,Ga)Se$_2$ and Cu(In,Ga)Se2 Thin Films Deposited by Three-Stage Coevaporation. *IEEE J. Photovoltaics* **4**, 447–451 (2014).
3. Edoff, M. *et al.* High Voc in (Cu,Ag)(In,Ga)Se$_2$ Solar Cells. *IEEE J. Photovoltaics* **7**, 1789–1794 (2017).
4. Edoff, M. *et al.* Post Deposition Treatments of (Ag,Cu)(In,Ga)Se$_2$ Thin Films for Solar Cells. *Conf. Rec. IEEE Photovolt. Spec. Conf.* 618–621 (2019) doi:10.1109/PVSC40753.2019.8981287.
5. Chirilă, A. *et al.* Potassium-induced surface modification of Cu(In,Ga)Se$_2$ thin films for high-efficiency solar cells. *Nat. Mater.* **12**, 1107–1111 (2013).
6. Muzzillo, C. P. Review of grain interior, grain boundary, and interface effects of K in CIGS solar cells: Mechanisms for performance enhancement. *Sol. Energy Mater. Sol. Cells* **172**, 18–24 (2017).
7. Valdes, N. H., Jones, K. J., Opila, R. L. & Shafarman, W. N. Influence of Ga and Ag on the KF Treatment Chemistry for CIGS Solar Cells. *IEEE J. Photovoltaics* **9**, 1846–1851 (2019).
8. Donzel-Gargand, O., Larsson, F., Törndahl, T., Stolt, L. & Edoff, M. Secondary phase formation and surface modification from a high dose KF-post deposition treatment of (Ag,Cu)(In,Ga)Se$_2$ solar cell absorbers. *Prog. Photovoltaics Res. Appl.* **27**, 220–228 (2019).
9. P. W. Li, R. A. Anderson, and R. H. P. Dielectric constant of CuInSe$_2$ by capacitance measurements. *J. Phys. Chem. Solids* **40(4)**, 333– 334 (1979).
10. Daniel Abou-Ras, Thomas Kirchartz & Rau, U. 'Capacitance Spectroscopy of Thin-Film Solar Cells' in Advanced Characterization Techniques for Thin Film Solar Cells. in 81–105 (WILEY-VCH Verlag GmbH & Co. KGaA, 2016).
11. Erslev, P., Hanket, G. M., Shafarman, W. N. & Cohen, D. J. Characterizing the effects of silver alloying in chalcopyrite CIGS with junction capacitance methods. *MRS Proc.* **1165**, 1165-M01-07 (2009).
12. Valdes, N., Lee, J. W. & Shafarman, W. Comparison of Ag and Ga alloying in low bandgap CuInSe$_2$ -based solar cells. *Sol. Energy Mater. Sol. Cells* **195**, 155–159 (2019).
13. Valdes, N. H., Lee, J. & Shafarman, W. N. Ag alloying and KF treatment effects on low bandgap CuInSe$_2$ solar cells. *IEEE J. Photovoltaics* **9**, 906–911 (2019).
14. Rau, U., Blank, B., Müller, T. C. M. & Kirchartz, T. Efficiency Potential of Photovoltaic Materials and Devices Unveiled by Detailed-Balance Analysis. *Phys. Rev. Appl.* **7**, 1–9 (2017).
15. Rau, U. & Werner, J. H. Radiative efficiency limits of solar cells with lateral band-gap fluctuations. *Appl. Phys. Lett.* **84**, 3735–3737 (2004).
16. Redinger, A. *et al.* Time resolved photoluminescence on Cu(In, Ga)Se$_2$ absorbers: Distinguishing degradation and trap states. *Appl. Phys. Lett.* **110**, 122104 (2017).
17. Ross, R. T. Some thermodynamics of photochemical systems. *J. Chem. Phys.* **46**, 4590–4593 (1967).
18. Krause, M. *et al.* Microscopic origins of performance losses in highly efficient Cu(In,Ga)Se$_2$ thin-film solar cells. *Nat. Commun.* **11**, 4189 (2020).
19. Henry, C. H. Limiting efficiencies of ideal single and multiple energy gap terrestrial solar cells. *J. Appl. Phys.* **51**, 4494–4500 (1980).
20. Abou-Ras, D. *et al.* Enhancements in specimen preparation of Cu(In,Ga)(S,Se)$_2$ thin films. *Micron* **43**, 470–474 (2012).